JOURNAL OF OPTOELECTRONICS AND ADVANCED MATERIALS Vol. 8, No. 1, February 2006, p. 13 - 19

Electrical properties of nanocrystalline silicon

MAGDALENA LIDIA CIUREA*
National Institute of Materials Physics, Bucharest-Magurele 077125, Romania

The transport properties of nanocrystalline silicon films are presented. The studies were performed on fresh and stabilized nanocrystalline porous silicon (nc-PS) and on Si/SiO_2 nanocomposite films. Current – voltage characteristics and the temperature dependence of the dark current were measured on both systems. From the current – voltage characteristics of the oxidized nc-PS, the Si – SiO_2 potential barrier was determined (2.2 eV). The Si/SiO_2 measurements proved that the main conduction mechanism for the nanodot systems is the field-assisted tunneling under Coulomb blockade. The quantum confinement was evidenced by the activation energies observed in the current – temperature characteristics and it was modeled by means of an infinite quantum well. The trapping – detrapping processes were studied by using the Optical Charging Spectroscopy (OCS) method: the traps are filled by illumination with a suitable wavelength at low temperature and the detrapping is produced by heating at a constant rate. The experimental investigations evidenced six trapping levels in nc-PS, four located at the surface/interface and two deep ones located in the bulk. The deepest level was observed only in oxidized samples. The modeling of the OCS trapping – detrapping processes allows for the determination of the characteristic parameters that cannot be directly obtained from the measurements.

(Received October 25, 2005; accepted January 26, 2006)

Keywords: Nanocrystalline silicon, Electrical transport, Quantum confinement

1. Introduction

The great interest aroused by the nanocrystaline silicon (nc-Si) has originated in the discovery of the nc-PS bright photoluminescence in the visible range at room temperature (RT) [1, 2], suggesting possible applications in optoelectronics [3, 4]. Later on, this hope was abandoned, but the very large and reactive internal surface of the nc-PS lead to other possible applications, such as gas sensors [5-8], or capacitors [9]. The photo-luminescence properties of the silicon nanodots embedded in amorphous silicon dioxide (Si/SiO_2 nanocomposites) [10] make them also very attractive for optoelectronics, especially for photonic crystals [11].

Different microstructure investigations of nc-PS films have shown various aspects, depending on the etching conditions, the crystallographic orientation and the silicon wafers doping [12-14]. High resolution images exhibits complex fractal geometry. Several techniques were used to prepare the nanostructured Si/SiO_2 films [15, 16], the structure of the films being dependent on the preparation method [17, 18].

The electrical transport properties of nc-Si and silicon-based nanostructures are determined mainly by their microstructure. To explain the different experimental results, various transport mechanisms were studied and therefore several models were proposed. For nc-PS and Si nanowires, hopping process at low temperatures with thermal activation at high temperatures [19], Poole-Frenkel tunneling [20], fractal percolation [21], generation-recombination phenomena in the depletion region [22], and dangling bonds governing the Al / nc-PS junction [23] were considered. Simple and Coulomb field-enhanced Fowler-Nordheim tunneling were used to model the carrier injection from the substrate of a nanocrystalline floating-gate MOS transistor [24], while Schottky tunneling was applied to the investigation of ultra-small diodes [25]. Poole-Frenkel tunneling was also taken into account for nc-Si/CaF_2 multilayer structures [26]. In the case of Si nanodots embedded in an amorphous SiO_2 matrix, the transport inside the nanodots is ballistic [27]. Tunneling under Coulomb blockade occur between nanodots [28, 29], the Coulomb blockade being one of the most important confinement effects for the electrical conduction mechanisms.

The quantum confinement produces both the enlargement of the band gap [30] and the breakdown of the momentum conservation rule [31], as well as the appearance of new energy levels. These levels introduce additional activation energies in the temperature dependence of the current [32 – 34] and supplementary optical transitions [31, 35].

The trapping phenomena in nc-Si were rather slightly studied [36], in spite of the fact that the traps play an important role in the non-equilibrium phenomena and that their concentration in nanocrystalline systems should be high (especially the surface ones).

This paper presents the results of our research group concerning the electrical properties of the fresh and stabilized nc-PS and Si/SiO_2 nanocomposite films. Section 2 deals with the preparation of the samples and the measurement techniques. The experimental results concerning the current – voltage and current – temperature characteristics, and the traps investigation, as well as their modeling, are presented in Section 3. In Section 4, the properties of the two kinds of materials are compared, while the last Section summarizes the conclusions.

2. Experimental

The nc-PS layers were prepared in our laboratory by electrochemical etching of p-type (100) Si wafers (5 – 15 Ω·cm resistivity) in HF (49%)-C_2H_5OH (1:1 volume ratio) under constant 5 – 15 mA/cm^2 current density, followed by the illumination *in situ* for 1.5 – 3 min with a Xenon lamp, cleaning and drying in air (fresh samples) [37 – 39]. The samples were then stabilized either by storing in ambient conditions for 1.5 years, in order to induce native oxidation, or by anodic oxidation. The film thickness is 5 – 35 μm. By investigating the microstructure of these samples [39], it resulted that they present a two-level porosity. The first porosity level is structured as a honeycomb-like system of alveolar columnar macropores (1.5 – 3 μm diameter, 70 % macroporosity) that cross the whole nc-PS thickness. The second porosity level appears in the alveolar walls (100 – 200 nm thickness), and it is formed by a nanowire network (1 – 5 nm diameter of the nanowires, 50 % nanoporosity of the walls) that keeps the crystallinity of the bulk.

Si/SiO_2 nanocomposite films were obtained by co-sputtering of Si and SiO_2 on rectangular quartz slides (13 cm length, 2 cm width) [40]. The nucleation of Si crystallites is achieved by the annealing of the films at 1100 °C for 30 min in a N_2 flow. Thus, films with variable volume concentration of nc-Si from practically x = 0 % to practically x = 100 % are deposited in a single run. The film thickness is 9 μm after 12 h sputtering. The microstructure investigations [41] clearly evidenced the presence of the nc-Si with mean diameter of 3 nm from the x = 20 % region of the Si/SiO_2 film. The crystallites appear with {111} facets if the [110] zone axis is well aligned. At higher nc-Si concentrations ($x \geq 50$ %), the mean diameter of the nanodots is around 5 nm and they tend to form chain networks. The majority of the nanocrystallites remain under 10 nm diameter, even at high concentrations ($x \geq 70$ %), and the amorphous silicon dioxide thickness does not exceed 5 nm between nanodots. The big crystallites (over 10 nm diameter) present lattice defects, like twins or staking faults.

The current – voltage characteristics at RT, the temperature dependence of the dark current (I – T) between liquid nitrogen temperature (LNT) and RT, and the discharge currents in the traps investigations were measured with a Keithley 642 electrometer, a Keithley 2000 multimeter, and an Agilent E3631A d.c. power supply. The trap charging process was performed by illuminating the samples with monochromatic light by using a Carl Zeiss Jena SPM 2 monochromator. Sandwich configuration (bottom Al / c-Si / nc-PS / top Al) was used for the nc-PS samples, with the semitransparent top electrode thermally evaporated at an angle of 15 ° with the nc-PS layer. The bottom electrode was annealed to become ohmic before the anodization process [38,39]. Contrariwise, coplanar configuration with 50 parallel aluminum contacts (7 mm long, 2 mm width, 2 mm distance) was used for the Si/SiO_2 samples, in order to measure different nc-Si concentration regions [40]. The annealing at 1100 °C does not allow the preparation of a sandwich configuration, due to the diffusion of the bottom electrode into the film.

3. Current – voltage characteristics

The I – V characteristics taken on nc-PS samples were measured at RT in the -30 – +30 V range [38,42]. Fig. 1 (Fig. 1, Ref. 38) presents the slow rectifying behavior of the fresh samples. This behavior is practically linear at low voltages (-5 – +5 V, see also [20]). Fig. 2 (Fig. 4, Ref. 38) presents the strong rectifying behavior of the stabilized samples, due to the oxidation of the nc-PS layer under the top electrode. Another proof of this oxidation is the MIS – like behavior of these samples in C – V characteristics (see [38]). The I – V curve is exponential up to 2.2 V in forward bias and then it becomes practically linear. The limit of 2.2 V gives the barrier height between Si and SiO_2. This barrier leads to a high series resistance and therefore to a linear behavior. A number of percolation thresholds can be observed in the quasi-linear region that confirms the model of the percolation network [39,42]. One can conclude that the I – V characteristics taken on nc-PS are typical for band conduction.

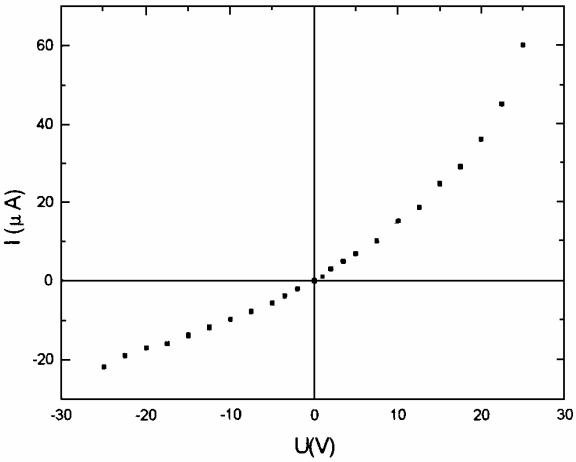

Fig. 1. I – V characteristic for fresh nc-PS sample at RT [38].

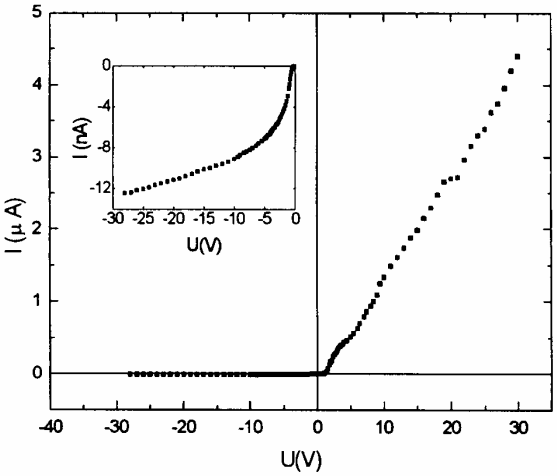

Fig. 2. I – V characteristic for stabilized nc-PS sample at RT [38].

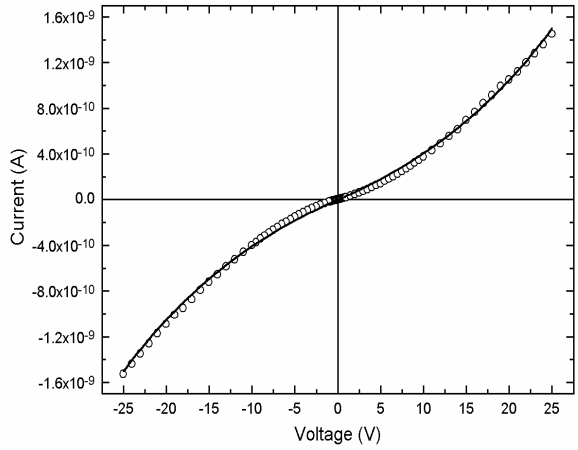

Fig. 3. I – V characteristic (circles) and theoretical fit (solid line) for Si/SiO$_2$ at RT [43].

Fig. 3 (Fig. 1, Ref. 43) presents a typical $I - V$ characteristic for Si/SiO$_2$ at RT (circles). The characteristic is practically symmetric (to be expected for a coplanar configuration) and superlinear.

It was already mentioned that the transport inside the nanodots is ballistic. The main conduction mechanism between nanodots is the high field-assisted tunneling ($U >> Nk_BT/e$, where N is the average number of tunneled barriers) [40, 43 – 45]. The tunneling current is given by the relation:

$$I = I_0 \cdot \mathrm{sign}(U) \cdot \left[\left(1 - \frac{|U|}{U_0}\right) \exp\left(-\alpha\sqrt{1 - \frac{|U|}{U_0}}\right) - \exp(-\alpha) \right]. \quad (1)$$

Here $I_0 \propto \varphi$ (φ is the average tunneled potential barrier height), $U_0 = N\varphi/e$, and $\alpha = \Delta s\sqrt{8m^*\varphi/\hbar^2}$ (Δs is the average barrier width). If one fits the experimental data represented in Fig. 3 with this relation, one obtains the solid line from the figure, where the fitting parameters are I_0 = 25.79 A, U_0 = 259.4 V and α = 24.26. Then, the linear correlation coefficient between the experimental data and the fitting formula is 99.95%. If one chooses for φ the value 2.2 eV, as in stabilized nc-PS [38, 42, 46], one obtains N = 118 and Δs = 1.6 nm. This proves that only a small part of the carrier path is covered by means of tunneling. However, this part introduces the biggest resistance and therefore dominates the characteristic.

From the comparison of the $I - V$ characteristics for the two kinds of materials, it results that the continuous crystalline paths (nanowire network, see [39, 42]) in nc-PS allow a band conduction mechanism, while the SiO$_2$ barriers between Si nanodots in the Si/SiO$_2$ nanocomposite systems imply a tunneling mechanism. The barrier height much greater than the carrier energy ($U_0 >> U$) proves that the only possible tunneling mechanism is the high field-assisted one.

4. Current – temperature characteristics

The $I - T$ characteristics for fresh nc-PS samples present an Arrhenius-like behavior with one activation energy on the whole temperature range, as one can see in Fig. 4 (Fig. 2, Ref. 38). The value of the activation energy is situated in the dispersion interval 0.49 – 0.55 eV and is independent on the bias polarity.

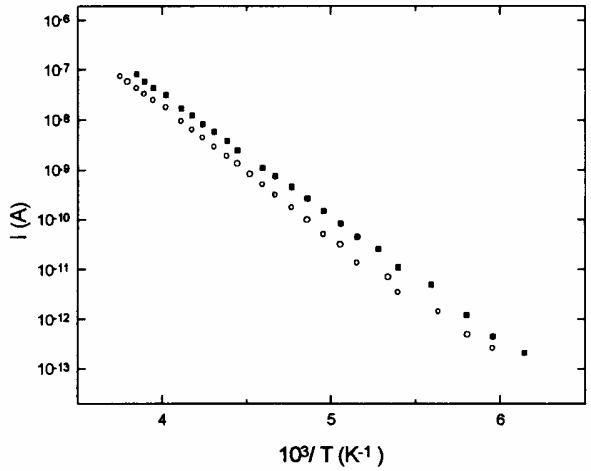

Fig. 4. I – T characteristics for fresh nc-PS sample: ○ U_a = 1 V ('+' on c-Si), ■ U_a = – 1 V ('+' on nc-PS) [38].

The characteristics measured on stabilized nc-PS samples present two activation energies, with an abrupt change of slope, as one can see in Fig. 5 (Fig. 5, Ref. 38). The value of the low temperature activation energy is situated in the dispersion interval 0.50 – 0.60 eV, slightly increased that the one found for fresh samples. At temperatures higher than about 280 K, a new activation energy, situated in the dispersion interval 1.20 – 1.80 eV, appears. The mean values of the two activation energies (E_{a1} = 0.55 ± 0.05 eV, E_{a2} = 1.50 ± 0.30 eV) are in a ratio of $R \equiv E_{a2}/E_{a1}$ = 2.73.

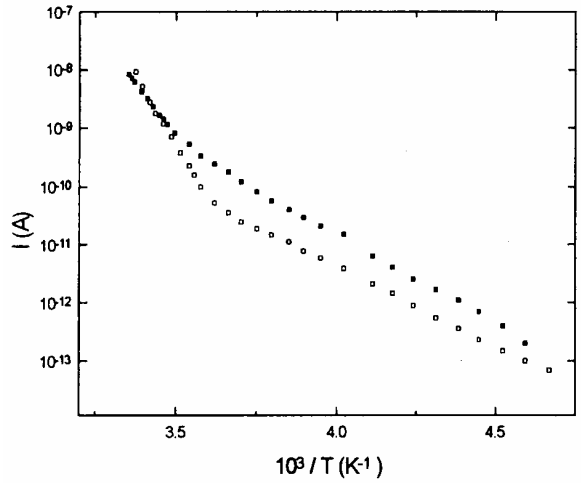

Fig. 5. I – T characteristics for stabilized nc-PS sample: ■ U_a = 2 V ('+' on c-Si), □ U_a = -2 V ('+' on nc-PS) [38].

Fig. 6 (Fig. 8, Ref. 47) presents the $I - T$ characteristics for Si/SiO_2 films, measured at x = 73 % region at 1, 5, and 25 V applied bias, in the temperature range 200 – 300 K [47]. The activation energy values are E_{a1} = 0.30 ± 0.01 eV and E_{a2} = 0.51 ± 0.01 eV for all biases, and their ratio is R = 1.70.

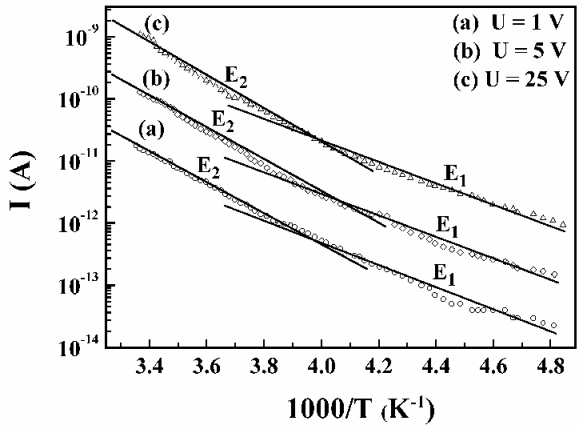

Fig. 6. I – T characteristics for Si/SiO_2 nanocomposite at x ≈ 73 %, at 1, 5 and 25 V [47].

The new levels induced by the quantum confinement in the band gap are due to the fact that the nanocrystal surface acts like the wall of a quantum well [38 – 40,42, 43,46 – 48]. The simplest model considers an infinite rectangular quantum well, the errors introduced by this approximation being under 2.5 % for sizes under 10 nm and barrier heights over 2 eV [38,46].

The nc-PS samples are structured in a nanowire network, as mentioned in Section 2. Then the electron Hamiltonian for a nanowire is the sum of a longitudinal 1D Bloch term and a transversal 2D infinite quantum well one. Under these conditions the electron energy is

$$E = \varepsilon_{n,k_z} + \frac{2\pi^2\hbar^2}{m^* d^2} x_{l,p}^2 = \left(\varepsilon_{n,k_z} + \frac{2\pi^2\hbar^2}{m^* d^2} x_{0,1}^2 \right) + \\ + \frac{2\pi^2\hbar^2}{m^* d^2} \left(x_{l,p}^2 - x_{0,1}^2 \right) \equiv \varepsilon_{n,k_z}^s + E_{l,p-1} \quad , \quad (2)$$

where

$$E_{l,p} = \frac{2\pi^2\hbar^2}{m^* d^2} \left(x_{l,p+1}^2 - x_{0,1}^2 \right) \quad (3)$$

is the discrete energy level induced by the 2D quantum well and ε_{n,k_z}^s is the shifted Bloch term (by convention, $E_{0,0} \equiv 0$), m^* is the transversal effective electron mass and d the effective diameter.

Both cylindrical and square prism shapes were analyzed for the nanowire symmetry [39,42,47], giving corresponding expressions for $x_{l,p}$. In both cases, l represents the orbital quantum number. Neither shape is correct, due to the tetragonal symmetry of the silicon, but they give good first approximations.

A similar analysis can be done for Si/SiO_2 nanocomposites, with the nanodots considered spherical. Due to their sizes (0D systems), one has no proper band structure and the electron energy is simply given by Eq. (3), with $x_{l,p}$ corresponding to the spherical symmetry [43,47,48].

From the relation (3), it results that the carrier concentration is proportional with $\exp(-E_a/k_BT)$, where the activation energy E_a is the absolute value of the difference between the energies of the last occupied confinement level and the following one. This leads to an Arrhenius-like behavior of the $I - T$ characteristic. When a level is filled up, the following begins to be excited and the activation energy value is modified. Then, by evaluating the ratio for the consecutive values of the activation energy and comparing them with the experiment, one can estimate the quantum levels and therefore the nanocrystallite sizes.

In the case of the nc-PS samples, the experimental ratio R = 2.73 is practically the mean of the values for the cylindrical and square symmetries, if one takes $E_{a1} = E_{0,1} - E_{0,0}$ and $E_{a2} = E_{0,2} - E_{0,1}$. The orbital momentum conservation is due to the symmetry of the electric field interaction. The corresponding nanowire diameter is d = 3.3 nm for fresh samples (cylindrical symmetry), in good agreement with the microstructure investigations. For stabilized samples, Eq. (2) leads to a 0.1 nm thinning induced by oxidation, which is not plausible. However, if one takes into account that the effective mass approximation, implicit in the previous analysis, is not valid for sizes under 5 nm [11,30] and if one considers the size dependence found by using the Linear Combination of Atomic Orbitals method [30], the thinning becomes one interatomic distance.

In the case of the Si/SiO_2 samples, the experimental ratio R = 1.70 also corresponds to $E_{a1} = E_{0,1} - E_{0,0}$ and $E_{a2} = E_{0,2} - E_{0,1}$, with a nanodot diameter d = 4.5 nm, in good agreement with the microstructure investigations.

It can be seen that the predictions of the infinite quantum well model are in good agreement with the experimental results for both 1D and 0D systems, in spite of the simplicity of the model.

5. Traps investigations

Optical Charging Spectroscopy (OCS) measurements of the trapping – detrapping phenomena in nc-PS consist of two successive steps [49,50]. In the first step, the sample is cooled down at LNT (quoted T_0 in the following) and then it is illuminated for 10 min with monochromatic light, in order to fill the traps. The illumination is performed either in open or in short circuit The used wavelengths were 0.5 μm (absorption coefficient $\alpha = 2 \times 10^3$ cm^{-1}) and 1.0 μm (α = 10 cm^{-1}) [51]. The illumination generates non-equilibrium carriers that diffuse into the sample with different mobilities, some of them being trapped. The traps are filled up under two

conditions: (i) the light intensity is high enough and the illumination time is long enough; (ii) the sample is thin compared to both the carrier diffusion and light absorption lengths. The trapped carriers generate a frozen-in electric field.

The second step starts with the switch off of the light. Then, the sample is connected to an electrometer and heated up to RT at a constant rate $\beta = dT/dt =$ 0.1 K/s. During the heating, the carriers trapped on different levels are successively released into the conduction and valence bands. The detrapped carriers move in the frozen-in electric field of the still trapped ones. The temperature dependence of this discharge current presents several positive and/or negative maxima and shoulders. This behavior is related to the discharge of the successive levels. The sign of the current is related to the sign of the frozen-in electric field, which depends on the consecutive discharge of trapped electrons and holes.

Fig. 7 (Fig. 1, Ref. 49) presents the discharge current versus temperature curves obtained on a fresh nc-PS sample. Five maxima and/or shoulders appear on both curves at approximately the same temperatures. In order to find out the activation energies of the associated trapping levels, the fractional heating procedure was used. The maximum No. 1 has an activation energy E_{a1} = 0.29 eV. The activation energy obtained for the following broad maximum (curve *a*) or shoulder (curve *b*) is situated in the 0.37–0.41 eV interval. This can be attributed to two trapping levels, 2' and 2", which are too close to one another to be separated. The maxima No. 1 and 2 (2'+2") have opposite signs, which means that at least one of the two levels, 2' or 2", traps opposite sign carriers with respect to level 1. The activation energy of maximum No. 3 (curve *b*) is E_{a3} = 0.47 eV (in curve *a*, this maximum is practically screened by the previous one). The shoulder and the maximum F on curves *a* and *b* respectively represent a false maximum. Such a maximum appears when a level is discharged in the opposite sign field of the next one. The activation energy of the last maximum is E_{a4} = 0.61 eV.

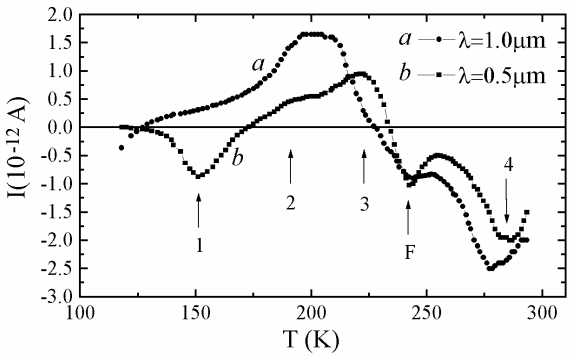

Fig. 7. Discharge currents for fresh nc-PS sample [49].

The discharge current versus temperature curves obtained on nc-PS samples stabilized by native or anodical oxidation are presented in Figs. 8 (Fig. 1, Ref. 52) and 9 (Fig. 2, Ref. 52). In these figures, the maxima 2', 2", 3, and 4 are renumbered 2, 3, 4, and 5. The maxima 1 to 4 are strongly reduced after native oxidation and practically disappear after anodical oxidation. This proves that they correspond to surface traps. A new maximum appears, with E_{a6} = 0.82 eV, for both kind of oxidized samples and the maximum 5 is reduced to a shoulder. However, both of them are much bigger than maxima 1 to 4, which shows that they correspond to bulk traps. The appearance of the last maximum after the oxidation also suggests that it is due to the oxidation-induced strains.

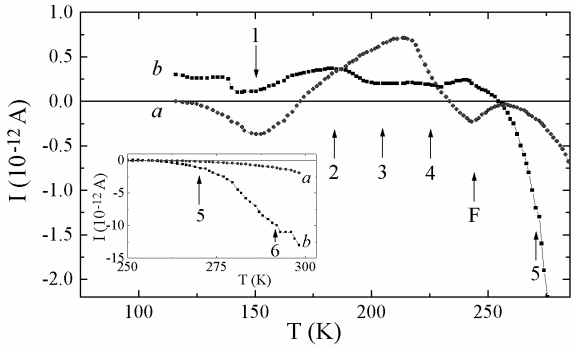

Fig. 8. Discharge currents for a – natively and b – anodically oxidized nc-PS samples; illumination wavelength λ = 0.5 μm [52].

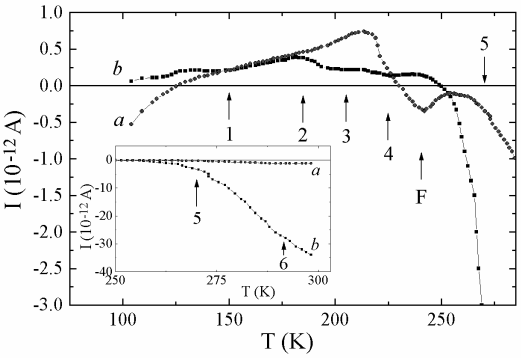

Fig. 9. Discharge currents for a – natively and b – anodically oxidized nc-PS samples; illumination wavelength λ = 1.0 μm [52].

The discharge current in OCS measurements is the sum of four terms [42, 49, 50, 52]. The main one, I_{ne}, is due to the movement of the non-equilibrium carriers released from traps in the frozen-in electric field of the still trapped ones:

$$I_{ne} = \frac{1}{2} A \Delta\sigma(T) E(d,T), \qquad (4)$$

where A and d are the top electrode area and nc-PS layer thickness,

$$\Delta\sigma(T) = e[\mu_p(T)\Delta p(T) + \mu_n(T)\Delta n(T)] \qquad (5)$$

is the conductivity of the released carriers, with concentrations Δp and Δn, and

$$E(d,T)=\frac{ed}{\varepsilon_0\varepsilon_r}[p_t(T)-n_t(T)] \quad (6)$$

is the frozen-in electric field of the still trapped carriers, with concentrations p_t and n_t (homogeneously distributed). This current is a square function of the traps concentrations, due to the fact that $\Delta p \propto p_t$ and $\Delta n \propto n_t$. The second term, I_e, which is significant at high temperatures only, is due to the movement of the equilibrium carriers in the same field:

$$I_e=\frac{1}{2}A\sigma_0(T)E(d,T). \quad (7)$$

The displacement current,

$$I_d=\frac{1}{2}A\varepsilon_0\varepsilon_r\beta\frac{\partial}{\partial T}E(d,T), \quad (8)$$

is two to four orders of magnitude smaller than the previous currents, while the diffusion current

$$I_D=\frac{A}{d}kT\{\mu_p[\Delta p(d,T)-\Delta p(0,T)]-\mu_n[\Delta n(d,T)-\Delta n(0,T)]\} \quad (9)$$

cancels because of the homogeneous distribution of the traps in our nc-PS samples. This model permits the evaluation of several traps parameters that are not directly measurable.

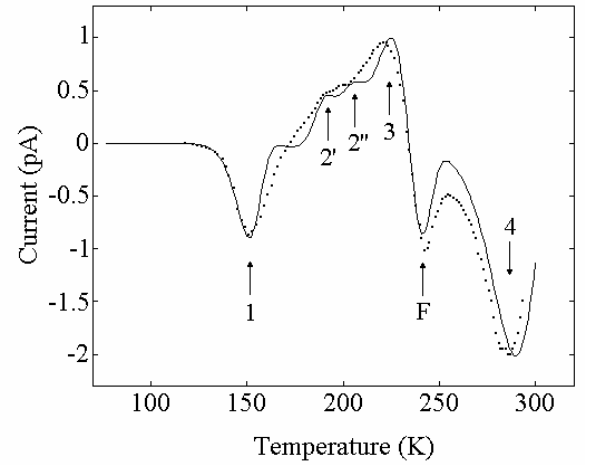

Fig. 10. Experimental (dotted line) and theoretical (continuous line) discharge currents for fresh nc-PS sample; illumination wavelength λ = 0.5 μm [50].

Fig. 10 (Fig. 4, Ref. 50) presents the results of the model applied to the discharge current in fresh nc-PS sample illuminated with λ = 0.5 μm. Maxima 1, 2', and 4 are due to trapped holes, while maxima 2" and 3 correspond to trapped electrons. This separation is related to the differences between the mobilities and effective masses for electrons and holes. The values obtained for the capture cross-sections ς, traps concentrations N_t, released carrier lifetimes τ and activation energies E_a are presented in Table 1 [50]. The errors in the determination of the activation energies are of the order of 1 %, much smaller than the experimental ones. This allows us to accept the splitting of the broad maximum 2 in two maxima (2' and 2") as corresponding to a real superposition of two distinct levels.

Table 1. The values of the parameters for the trapping levels in fresh nc-PS.

No.	ς (10^{-18} m^2)	N_t (10^{17} m^{-3})	τ (ns)	E_a (eV)	
				Model	Exp.
1	3.0	18.0	50	0.30	0.29
2'	3.0	15.0	50	0.37	0.37–0.41
2"	1.5	2.5	50	0.41	
3	0.9	14.0	50	0.47	0.47
4	3.0	0.85	150	0.61	0.61

The coplanar configuration of the Si/SiO_2 nanocomposites does not allow OCS measurements, due to the vanishingly small frozen-in electric field. Besides, the conduction currents have to be replaced by tunneling currents, at least three orders of magnitude smaller (see Section 3).

6. Conclusions

To summarize, the electrical properties of nanocrystalline silicon are determined by the quantum confinement of the carriers, the transport mechanisms, and the surface effects.

The quantum confinement appears as typical for all the nanocrystalline systems. Its main effect is the appearance of new energy levels that are evidenced in the $I - T$ characteristics. These levels can be evaluated with good accuracy on the basis of an infinite quantum well model.

The transport mechanism depends on the dimensionality of the system. While for 1D systems (nc-PS) the transport mechanism is the band conduction, for 0D ones (Si/SiO_2) the dominant mechanism is the high field-assisted tunneling, the corresponding model giving a good agreement with the experimental data.

The large and reactive surface / interface of the nanocrystalline systems determines the appearance of large surface / interface trap concentrations. The stabilization of the Si surface by oxidation produces strains that induce bulk trapping centers. The model of the OCS discharge current in 1D systems is in good agreement with the experiment and permits the evaluation of several traps parameters that are not directly measurable.

References

[1] L. T. Canham, Appl. Phys. Lett. **57,** 1046 (1990).
[2] V. Lehmann, V. Gösele, Appl. Phys. Lett. **58,** 8621 (1991).
[3] B. Hamilton, Semicond. Sci. Technol. **10,** 1187 (1995).
[4] "Properties of Porous Silicon" edited by L. T. Canham, EMIS Datareviews Series No. 18, INSPEC, London (1997).
[5] T. Taliercio, M. Dilhan, E. Massone, A. M. Gué, B. Fraisse, and A. Foucaran, Thin Solid Films **255,** 310 (1995).
[6] C. Dücsö, N. Q. Khanh, Z. Horváth, I. Bársony, M. Utriainen, S. Lehto, M. Nieminen, and I. Niinistö, J. Electrochem. Soc. **143,** 683 (1995).
[7] Z. Gaburro, P. Bettotti, M. Saiani, L. Pavesi, Appl. Phys. Lett. **85**, 555 (2004).
[8] Z. Gaburro, C. J. Oton, L. Pavesi, Appl. Phys. Lett. **84**, 4388 (2004).
[9] V. Lehman, W. Hönlein, H. Reisinger, A. Spitzer, H. Wendt, J. Willer, Thin Solid Films **276,** 138 (1996).
[10] J. P. Wilcoxon, G. A. Samara, P. N. Provencio, Phys. Rev. B **60**, 2704 (1999).
[11] J. Heitmann, R. Scholz, M. Schmidt, M. Zacharias, J. Non-Cryst. Solids **299-302**, 1075 (2002).
[12] I. Barbezier, A. Halimaoui, J. Appl. Phys. **74,** 5421 (1993).
[13] A. G. Cullis, L. T. Canham, P. D. J. Calcott, J. Appl. Phys. **82,** 909 (1997).
[14] M. J. Winton, S. D. Russell, R. Gronsky, J. Appl. Phys. **82,** 436 (1997).
[15] Y. Wakayama, T. Inokuma, S. Hasegawa, J. Crystal Growth **183**, 124 (1998).
[16] M. Dovrat, Y. Oppenheim, J. Jedrzejewski, I. Balberg, and A. Sa'ar, Phys. Rev. B **69**, 155311 (2004).
[17] X. Zhang, G. Han, Thin Solid Films **415**, 5 (2002).
[18] R. Q. Zhang, T. S. Chu, H. F. Cheung, N. Wang, S. T. Lee, Mater. Sci. Eng. C **16**, 31 (2001).
[19] N. Koshida, H. Koyama, Mater. Res. Soc. Symp. Proc. **283,** 337 (1993).
[20] M. Ben-Chorin, F. Möller, F. Koch, Phys. Rev. B **49,** 2981 (1994).
[21] M. Ben-Chorin, F. Möller, F. Koch, Phys. Rev. B **51,** 2199 (1995).
[22] D. B. Dimitrov, Phys. Rev. B **51,** 1562 (1995).
[23] D. Stievenard, D. Deresmes, Appl. Phys. Lett. **67,** 1570 **(**1995).
[24] R. J. Walters, G. I. Bourianoff, H. A. Atwater, Nature Mater. - Adv. Online Public. doi: 10.1038/nmat1307 (2005).
[25] G. D. J. Smit, S. Rogge, T. M. Klapwijk, Appl. Phys. Lett. **81**, 3852 (2002).
[26] V. Ioannou-Sougleridis, T. Ouisse, A. G. Nassiopoulou, F. Bassani, F. Arnaud d'Avitaya, J. Appl. Phys. **89**, 610 (2001).
[27] T. V. Torchynska, J. Appl. Phys. **92**, 4019 (2002).
[28] D. Toker, D. Azulay, N. Shimoni, I. Balberg, O. Millo, Phys. Rev. B **68**, 041403(R) (2003).
[29] M. R. Reshotko, A. Sa'ar, and I. Balberg, Phys. Status Solidi A **197**, 113 (2003).
[30] C. Delerue, G. Allan, and M. Lannoo, Phys. Rev. B **48**, 11024 (1993).
[31] J. Heitmann, F. Müller, L. X. Yi, M. Zacharias, D. Kovalev, F. Eichhorn, Phys. Rev. B **69**, 195309 (2004).
[32] Y. L. He, X. N. Liu, Z. C. Wang, G. X. Cheng, L. C. Wang, S. D. Yu, Sci. China, Ser. A **36**, 248 (1993).
[33] G. Y. Hu, R. F. O'Connell, Y. L. He, M. B. Yu, J. Appl. Phys. **78,** 3945 (1995).
[34] Y. L. He, Y. Y. Wei, G. Z. Zhang, M. B. Yu, M. Liu, J. Appl. Phys. **82,** 3408 (1997).
[35] D. Kovalev, H. Heckler, G. Polisski, F. Koch, Phys. Status Solidi (b) **215**, 871 (1999).
[36] D. A. Faux, J. R. Downes, E. P. O'Reilly, J. Appl. Phys. **82**, 3754 (1997).
[37] M. L. Ciurea, E. Pentia, A. Manea, A. Belu-Marian, I. Baltog, Phys. Stat. Sol. (b) **195,** 637 (1996).
[38] M. L. Ciurea, I. Baltog, M. Lazar, V. Iancu, S. Lazanu, E. Pentia, Thin Solid Films **325,** 271 (1998).
[39] M. L. Ciurea, V. Iancu, V. S. Teodorescu, L. C. Nistor, M. G. Blanchin, J. Electrochem. Soc. **146,** 3516 (1999).
[40] V. Iancu, M. Draghici, L. Jdira, M. L. Ciurea, J. Optoelectron. Adv. Mater. **6**, 53 (2004).
[41] V. S. Teodorescu, M. L. Ciurea, V. Iancu, M. G. Blanchin, Proc. IEEE CN 04TH8748, Int. Semicond. Conf. CAS 2004, Sinaia, October 2004, **1**, 59 (2004).
[42] M. L. Ciurea, V. Iancu, Proc. IEEE CN 00TH8486, Int. Semicond. Conf. CAS 2000, Sinaia, October 2000, **1**, 55 (2000).
[43] V. Iancu, L. Jdira, M. Draghici, M. R. Mitroi, I. Balberg, M. L. Ciurea, Proc. IEEE CN 03TH8676, Int. Semicond. Conf. CAS 2003, Sinaia, October 2003, **1**, 83 (2003).
[44] J. G. Simmons, J. Appl. Phys. **34**, 1793 (1963).
[45] B. Abeles, P. Sheng, M. D. Coutts, Y. Arie, Adv. Appl. Phys. **24**, 407 (1975).
[46] V. Iancu, M. L. Ciurea, Solid State Electron. **42**, 1893 (1998).
[47] M. L. Ciurea, Proc. Third Int. Conf. on Powder Metallurgy, Sinaia, July 2005, **1**, 123 (2005).
[48] M. L. Ciurea, J. Optoelectron. Adv. Mater. **7**, 2341 (2005).
[49] M. L. Ciurea, M. Draghici, S. Lazanu, V. Iancu, A. Nasiopoulou, V. Ioannou, and V. Tsakiri, Appl. Phys. Lett. **76**, 3067 (2000).
[50] V. Iancu, M. L. Ciurea, M. Draghici, J. Appl. Phys. **49**, 216 (2003).
[51] D. Kovalev, G. Polisski, M. Ben-Chorin, J. Diener, F. Koch, J. Appl. Phys. **80**, 5978 (1996).
[52] M. Draghici, M. Miu, V. Iancu, A. Nassiopoulou, I. Kleps, A. Angelescu, M. L. Ciurea, Phys. Stat. Sol. (a) **182,** 239 (2000).

Invited Paper

*Corresponding author: ciurea@infim.ro